Results

The haploid *MYCN*, *DDX1*, and *NAG* gene copy number

Seventy-two of 113 tumors examined had *MYCN* amplification. Forty-one tumors were *MYCN*-unamplified; 17 in stages 1, 2 or 4S, nine in stage 3, and 15 in stage 4. Twenty-five and 16 patients were aged <18 and ≥18 months at diagnosis, respectively. Seven of 41 patients died of disease, while all 34 survivors are free of disease. Patients with *MYCN*-amplified NB included four with stage 1, two with stage 2, two with stage 4s, 12 with stage 3, and 52 patients with stage 4 disease. Of 72 patients with *MYCN*-amplified tumor, 45 patients died of disease, while 25 of 27 survivors are free of disease. The follow-up period for *MYCN*-amplified survivors ranged from 17 to 93 months.

In 72 *MYCN*-amplified NBs, *DDX1*, and *NAG* genes were found to be co-amplified in 49 (68.1%) and 19 (26.4%) tumors, respectively (Fig. 1a, b). All 19 tumors with *NAG* amplification had also *DDX1* amplification. Forty-one tumors without *MYCN* amplification were unamplified for *DDX1* and *NAG*. By plotting precise gene copy numbers of *MYCN* and *DDX1*, and *MYCN* and *NAG* of each tumor on the same graphs, we found for the first time that NB with lower copies of *MYCN* amplification tended to a more frequent *DDX1* and *NAG* co-amplification than those with higher copies of *MYCN*. For evaluating the frequency of *DDX1* and *NAG* co-amplification, it proved appropriate to discriminate NBs with <40 copies of *MYCN* amplification from those with ≥40 copies of *MYCN* (*DDX1*, $p = 0.00058$; *NAG*, $p = 0.0242$, χ^2 for independence test) (Fig. 1a, b).

Overall survival of patients with *MYCN*-amplified NB with or without *DDX1* and *NAG* co-amplification

For the 72 patients with *MYCN*-amplified NB, no statistically significant difference in survival probability was found among three gene co-amplification statuses, patients with tumor with *MYCN* amplification alone (*MYCN* alone), those with *DDX1* co-amplification alone (*MYCN* + *DDX1*), and those with both *DDX1* and *NAG* co-amplification (*MYCN* + *DDX1* + *NAG*) (*MYCN* alone versus *MYCN* + *DDX1*, $p = 0.465$; *MYCN* alone versus *MYCN* + *DDX1* + *NAG*, $p = 0.719$; *MYCN* + *DDX1* versus *MYCN* + *DDX1* + *NAG*, $p = 0.148$, log-rank test) (Fig. 2). We found no significant difference in overall survival between patients with tumor with *MYCN* amplification alone and those with *DDX1*-co-amplified NB regardless of *NAG* co-amplification ($p = 0.763$, log-rank test).

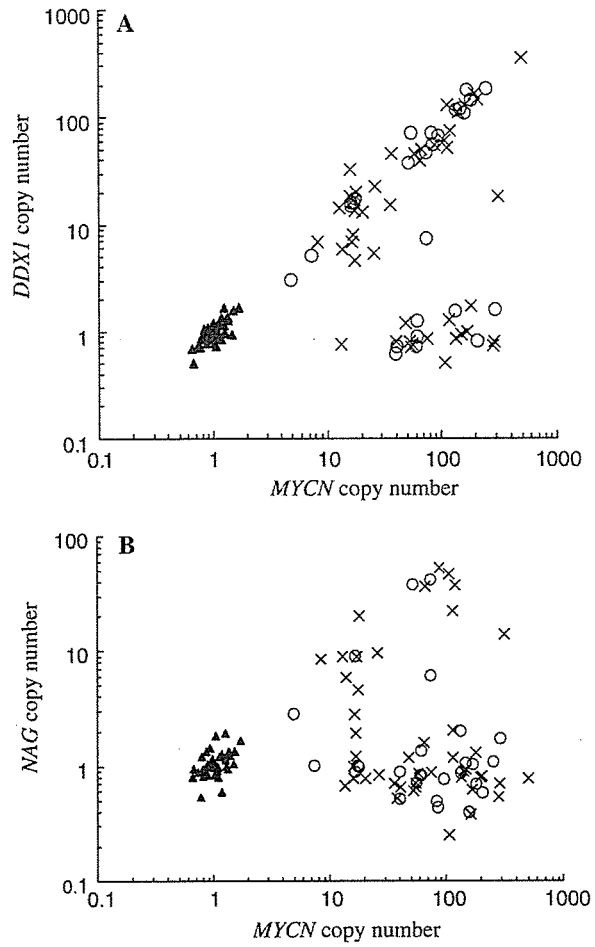

Fig. 1 The haploid *MYCN* and *DDX1* gene copy numbers (**a**), and *MYCN* and *NAG* gene copy numbers (**b**) in 113 NBs were determined by real-time q-PCR. *Open circle*, survivors with *MYCN* amplification ($n = 27$); *cross*, nonsurvivors with *MYCN* amplification ($n = 45$); *filled triangle*, patients without *MYCN* amplification ($n = 41$)

Relation of gene co-amplification status to disease stage or age at diagnosis

Table 1 shows the gene co-amplification status, disease stage and age at diagnosis of 72 patients with *MYCN*-amplified NB. Recently, an age cut-off higher than 12 months has been proposed as a prognostic predictor for comparison of survival rate in NB, suggesting an appropriate age cut-off of 18 months (London et al. 2005).

None of the gene co-amplification statuses had a significant correlation with disease stage (stages 1, 2, 3, and 4s versus stage 4) or age at diagnosis (<18 months versus ≥18 months) (data not shown), with the exception of *NAG*, which tended toward a more frequent co-amplification with *MYCN* in stage 4 (17/52, 32.7%)

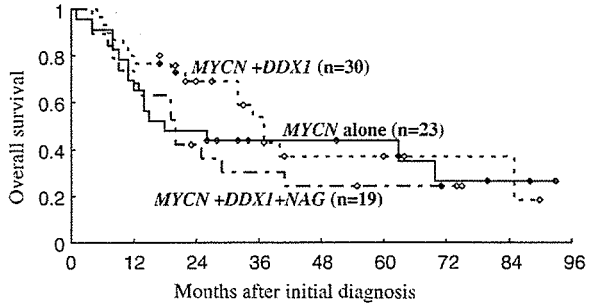

Fig. 2 Overall survival for patients with *MYCN*-amplified NB with or without *DDX1* and *NAG* co-amplification. No statistically significant difference in survival probability was found among three gene co-amplification statuses (*MYCN* alone versus *MYCN* + *DDX1*, $p = 0.465$; *MYCN* alone versus *MYCN* + *DDX1* + *NAG*, $p = 0.719$; *MYCN* + *DDX1* versus *MYCN* + *DDX1* + *NAG*, $p = 0.148$, log-rank test)

Table 1 Gene co-amplification status, disease stage and age at diagnosis of 72 patients with *MYCN*-amplified NB. There was no significant correlation between any gene co-amplification status and disease stage (stages 1, 2, 3, and 4s versus stage 4) or age at diagnosis among 72 patients with *MYCN*-amplified NB, with the exception of *NAG*, which tended toward a more frequent co-amplification with *MYCN* in stage 4 compared with stages 1, 2, 3, and 4s ($p = 0.0504$, χ^2 for independence test)

	Stage			Age (months)	
	1, 2 and 4s	3	4	<18	≥18
MYCN alone	4	4	15	10	13
MYCN+DDX1	4	6	20	11	19
MYCN+ DDX1+NAG	0	2	17	10	9
Total	8	12	52	31	41

compared with stages 1, 2, 3, and 4s (2/20, 10.0%) ($p = 0.0504$, χ^2 for independence test).

The expression level of *MYCN*, *DDX1*, and *NAG*

We determined the precise expression levels of *MYCN*, *DDX1*, and *NAG* in 108 of 113 NBs. Sixty-seven of 108 tumors had *MYCN* amplification. The *MYCN*-amplified tumors had a significantly higher expression level of *MYCN* compared with *MYCN*-unamplified tumors ($p = 8.22 \times 10^{-15}$, Mann–Whitney's *U*-test). None of the *MYCN*-unamplified tumors showed an overexpression of *MYCN*, *DDX1*, and *NAG* (data not shown). We classified *DDX1* or *NAG* gene expression levels higher than the highest in *MYCN*-unamplified tumors as enhanced.

In general, *DDX1* expression increased according to the *DDX1* copy number (Fig. 3a). The expression level of *DDX1* in tumors with *MYCN* amplification alone was as low as that without *MYCN* amplification. Enhanced DDX1 expression had no significant correlation with prognosis ($p = 0.925$, log-rank test).

The expression level of *NAG* in *NAG* co-amplified tumors was significantly higher than that in tumors without *NAG* co-amplification ($p = 5.77 \times 10^{-6}$, Mann–Whitney's *U*-test); however, *NAG* amplification was not necessarily accompanied with enhanced *NAG* expression (Fig. 3b). Enhanced *NAG* expression had no significant relation to disease stage (stage 1, 2, 3, and 4s versus stage 4) ($p = 0.462$, Fisher's exact probability test) or clinical outcome ($p = 0.0915$, log-rank test).

Relation of *DDX1* and *NAG* gene expression statuses to survival probability for patients with *MYCN*-amplified NB

None of the gene expression statuses had a significant correlation with disease stage and with survival for patients aged <18 months (data not shown).

In 41 patients with *MYCN*-amplified NB aged ≥18 months, those with tumor with enhanced *DDX1* expression and low-*NAG* expression had a significantly better outcome than those with low-*DDX1* expression or enhanced *NAG* expression ($p = 0.0245$, log-rank test) (Fig. 4a, b). The 16 tumors with enhanced *DDX1* and low-*NAG* expression included one with stage 2, four with stage 3, and 11 tumors with stage 4. All 16 tumors had *MYCN* and *DDX1* co-amplification without *NAG* amplification.

Discussion

Amplification of the *MYCN* gene is strongly associated with the rapid progression of NB and advanced disease stage (Brodeur et al. 1984; Seeger et al. 1985). The prognosis of patients with stage 4 tumors with *MYCN* amplification had been extremely poor. In 1999, Kaneko et al. reported treatment results with improved survival rate of patients with advanced NB aged 1 year or older treated with an intensive induction and consolidation chemotherapy regimens (Kaneko et al. 1999). With the use of a more intensive induction regimen followed by hematopoietic stem cell transplantation for *MYCN*-amplified stage 4 patients, survival curves for those with or without *MYCN* amplification appeared similar. In other words, the prognosis of patients with stage 4 NB without *MYCN* amplification remained poor (Kaneko et al. 2002). Their assessment of *MYCN* amplification status was based on the Southern blot technique. Measuring an accurate *MYCN* copy number in tumors is essential in

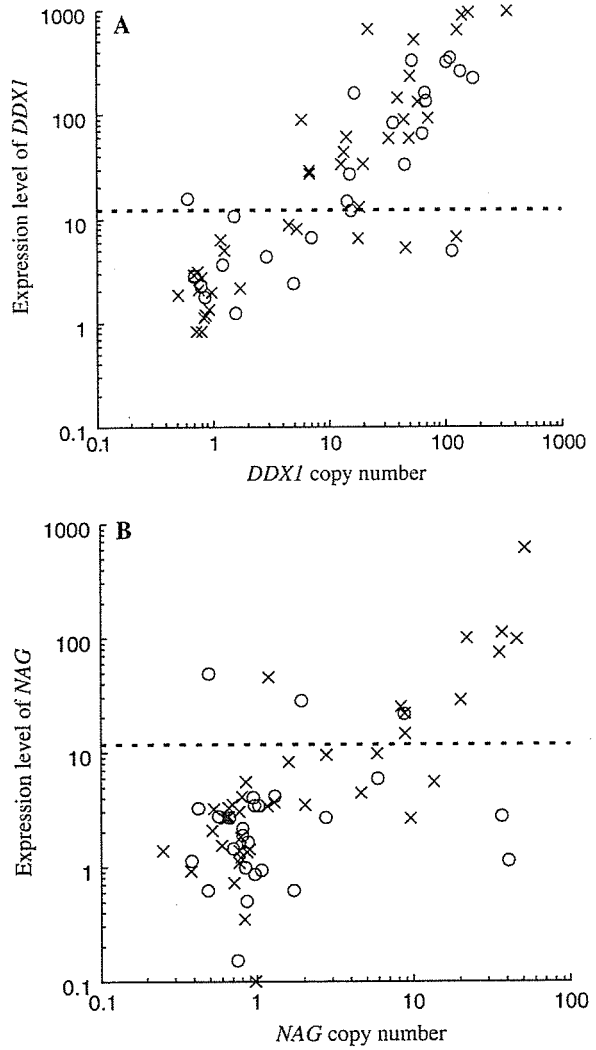

Fig. 3 Gene copy number and gene expression level of *DDX1* (**a**) and *NAG* (**b**) in 67 *MYCN*-amplified NBs. *Open circle*, survivors with *MYCN* amplification ($n = 26$); *cross*, nonsurvivors with *MYCN* amplification ($n = 41$); *dotted line*, the highest expression level of *DDX1* (**a**) or *NAG* (**b**) in *MYCN*-unamplified NBs

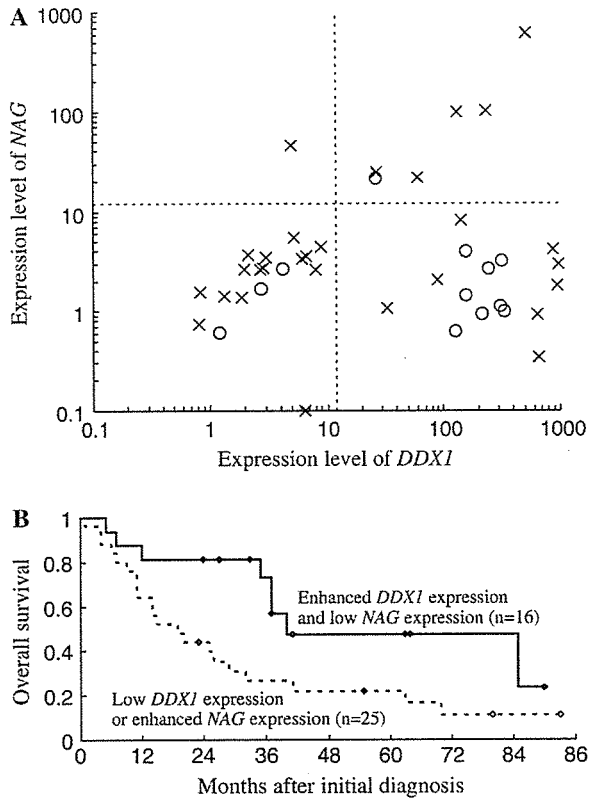

Fig. 4 **a** Expression level of *DDX1* and *NAG* mRNA in 41 *MYCN*-amplified NBs from patients aged ≥18 months. *Open circle*, survivors with *MYCN* amplification ($n = 12$); *cross*, nonsurvivors with *MYCN* amplification ($n = 29$); *dotted lines*, the highest expression levels of *DDX1* and *NAG* in *MYCN*-unamplified NBs. **b** In the 41 patients with *MYCN*-amplified NB aged ≥18 months, those with tumor with enhanced *DDX1* expression and low-*NAG* expression showed a significantly better outcome than those with low-*DDX1* expression or enhanced *NAG* expression ($p = 0.0245$, log-rank test)

order to select the optimal treatment and improve survival for patients with advanced NB. Assays for the rapid and accurate quantification of *MYCN* copy number and *MYCN* expression level in NB have been developed by real-time q-PCR or q-RT-PCR method with TaqMan probe (Raggi et al. 1999; Tajiri et al. 2001; De Preter et al. 2002). Tanaka et al. reported that in their highly sensitive analysis by a q-PCR method combined with FISH, cases with more than two *MYCN* gene dosages (*MYCN/p53* ≥2.0) were significantly associated with unfavorable prognostic factors (Tanaka et al. 2004). In our study, we did not investigate NBs with a haploid *MYCN* gene copy number of between two and five.

Recently, Scott et al. found that the 7.3 kb transcript of the *NAG* gene with 52 exons, which is predominantly expressed in NB, covers 420 kb of genomic DNA. They proposed that probes for Southern blot or FISH studies, or primers used for PCR-based methods, should include the 3′ end of the *NAG* gene over 400 kb away from *DDX1* (Scott et al. 2003b). The primers and TaqMan probe we designed were located on the 3′ end of the *NAG* gene, on exon 52, and the frequency of *NAG* co-amplification with *MYCN* was in accordance with that reported by Scott et al.

It is thought that a low copy number of *MYCN* in *MYCN*-amplified human NB cells is correlated with a low degree of recombination and large amplicon size (Amler and Schwab 1989). Consistent with the findings by Amler and Schwab, we found for the first time that NB with lower copies of *MYCN* amplification tended

to a more frequent *DDX1* and *NAG* co-amplification than those with higher copies of *MYCN*. For evaluating the frequency of *DDX1* and *NAG* co-amplification, it proved appropriate to discriminate NBs with <40 copies of *MYCN* amplification from those with ≥40 copies of *MYCN*. The information obtained from these observations may be different from a recent suggestion by De Preter et al. that the process of co-amplification within the *MYCN* amplicon occurs coincidentally, and is not subject to selection (De Preter et al. 2005).

The prognostic significance of DDX1 co-amplification with MYCN has remained unclear. Squire et al. analyzed 13 *MYCN*-amplified patients and showed a trend toward a worse clinical outcome with *DDX1* co-amplification (Squire et al. 1995). George et al. reported that with the exclusion of patients with 4S disease, those with *DDX1* co-amplification had a significantly shorter mean disease-free interval compared with *MYCN* amplification alone (George et al. 1997). However, they described that there was no significant difference in the proportion of survivors in these two groups. In contrast, Weber et al. reported that *DDX1* co-amplification correlated with an improved patient survival in 98 *MYCN*-amplified NB (Weber et al. 2004). In our study of 72 patients with *MYCN*-amplified NB, there was no significant difference in survival probability between patients with *DDX1*-co-amplified NB and those with tumor with *MYCN* amplification alone. The result was similar to those reported by Manohar et al. and De Preter et al. (Manohar et al. 1995; De Preter et al. 2002, 2005).

The *NAG* tended toward a more frequent co-amplification with *MYCN* in stage 4 compared with other stages, in contrast to the result of a significant association of *NAG* co-amplification with low-stage disease by Scott et al. (2003b). The difference was probably caused by the lower frequency of *NAG* co-amplification with *MYCN*. Amplification of *NAG* was not necessarily accompanied with enhanced *NAG* expression, and *NAG* expression level in *MYCN*-amplified tumors showed no significant relation to disease stage. The relationship between RNA expression levels of *DDX1* or *NAG* and clinical outcome for patients with *MYCN*-amplified NB has hardly been studied. Weber et al. reported that a high expression level of *DDX1* was associated with a trend toward a better survival probability while *NAG* expression was not correlated with prognosis (Weber et al. 2004). They drew the result using RNAs from 19 *MYCN*-amplified NB samples. We analyzed *DDX1* and *NAG* gene expression in 67 *MYCN*-amplified NB. Enhanced *DDX1* and *NAG* expression had no significant correlation with prognosis, respectively.

For the discrimination of prognosis for patients with NB, an age cut-off of 12 months was adopted worldwide. However, the International Neuroblastoma Pathology Classification, established for the prognostic evaluation of patients with neuroblastic tumors, has incorporated age factor of 18 months in the system (Shimada et al. 2001; Sano et al. 2006). The Children's Cancer Group in the USA has already chosen the 18 months as an age cut-off (Schmidt et al. 2005). Recent evidence supports the age cut-off ranging 15–18 months based on the results from the German analysis and two Children's Oncology Group analyses (London et al. 2005). In our study, the *DDX1* and *NAG* gene expression status in *MYCN*-amplified NBs revealed an age cut-off of 18 months to be an appropriate prognostic predictor of survival. We found that older patients with enhanced *DDX1* expression and low-*NAG* expression had a significantly better prognosis than those with low-*DDX1* expression or enhanced *NAG* expression. These findings indicate that, for *MYCN*-amplified NB from patients aged ≥18 months, both enhanced *DDX1* expression and low-*NAG* expression may be associated with a better response to intensive therapy. It is also possible to suggest a subset of NB in which enhanced *DDX1* and low-*NAG* expression consequent to *MYCN* and *DDX1* co-amplification without *NAG* amplification contributes to patient survival.

A larger cohort of patients and longer follow-up period using an age cut-off of 18 months will be required to clarify the clinical and prognostic significance of the expression status of both *DDX1* and *NAG* genes with *MYCN*.

References

Amler LC, Schwab M (1989) Amplified N-myc in human neuroblastoma cells is often arranged as clustered tandem repeats of differently recombined DNA. Mol Cell Biol 9:4903–4913

Beheshti B, Braude I, Marrano P, Thorner P, Zielenska M, Squire JA (2003) Chromosomal localization of DNA amplifications in neuroblastoma tumors using cDNA microarray comparative genomic hybridization. Neoplasia 5:53–62

Bleoo S, Sun X, Hendzel MJ, Rowe JM, Packer M, Godbout R (2001) Association of human DEAD box protein DDX1 with a cleavage stimulation factor involved in 3'-end processing of pre-MRNA. Mol Biol Cell 12:3046–3059

Brodeur GM, Seeger RC, Schwab M, Varmus HE, Bishop JM (1984) Amplification of N-myc in untreated human neuroblastoma correlates with advanced disease stage. Science 224:1121–1124

Brodeur GM, Seeger RC (1986) Gene amplification in human neuroblastoma: basic mechanisms and clinical implications. Cancer Genet Cytogenet 19:101–111

Chen HC, Lin WC, Tsay YG, Lee SC, Chang CJ (2002) An RNA helicase, DDX1, interacting with poly(A) RNA and hetero-

geneous nuclear ribonucleoprotein K. J Biol Chem 277: 40403–40409

Chomczynski P, Sacchi N (1987) Single-step method of RNA isolation by acid guanidium thiocyanate-phenol-chloroform extraction. Anal Biochem 162:156–159

De Preter K, Spelemam F, Combaret V, Lunec J, Laureys G, Eussen BH, Francotte N, Board J, Pearson AD, De Paepe A, Van Roy N, Vandesompele J (2002) Quantification of MYCN, DDX1, and NAG gene copy number in neuroblastoma using a real-time quantitative PCR assay. Mod Pathol 15:159–166

De Preter K, Spelemam F, Combaret V, Lunec J, Board J, Pearson A, De Paepe A, Van Roy N, Laureys G, Vandesompele J (2005) No evidence for correlation of DDX1 gene amplification with improved survival probability in patients with MYCN-amplified neuroblastomas. J Clin Oncol 23:3167–3168

De Valoir T, Tucker MA, Belikoff EJ, Camp LA, Bolduc C, Beckingham K (1991) A second maternally expressed Drosophila gene encodes a putative RNA helicase of the DEAD box family. Proc Natl Acad Sci USA 88:2113–2117

George RE, Kenyon R, McGuckin AG, Kohl N, Kogner P, Christiansen H, Pearson AD, Lunec J (1997) Analysis of candidate gene co-amplification with MYCN in neuroblastoma. Eur J Cancer 33:2037–2042

Godbout R, Squire JA (1993) Amplification of a DDX1 box protein gene in retinoblastoma cell lines. Proc Natl Acad Sci USA 90:7578–7582

Godbout R, Packer M, Katyal S, Bleoo S (2002) Cloning and expression analysis of the chicken DEAD box gene DDX1. Biochim Biophys Acta 1574:63–71

Iost I, Dreyfus M (1994) mRNAs can be stabilized by DEAD-box proteins. Nature 372:193–196

Kaneko M, Tsuchida T, Uchino J, Takeda T, Iwafuchi M, Ohnuma N, Mugishima H, Yokoyama J, Nishihira H, Nakada K, Sasaki S, Sawada T, Kawa K, Nagahara N, Suita S, Sawaguchi S (1999) Treatment results of advanced neuroblastoma with the first Japanese Study Group Protocol. J Pediatr Hematol Oncol 21:190–197

Kaneko M, Tsuchida T, Mugishima H, Ohnuma N,Yamamoto K, Kawa K, Iwafuchi M, Sawada T, Suita S (2002) Intensified chemotherapy increases the survival rates in patients with stage 4 neuroblastoma with MYCN amplification. J Pediatr Hematol Oncol 24:613–621

Kitajima Y, Yatsuki H, Zhang R, Matsuhashi S, Hori K (1994) A novel human homolog of a DEAD-box RNA helicase family. Biochem Biophys Res Commun 199:748–754

Kuroda H, White PS, Sulman EP, Manohar CF, Reiter JL, Cohn SL, Brodeur GM (1996) Physical mapping of the DDX1 gene to 340 kb 5' of MYCN. Oncogene 13:1561–1565

London WB, Boni L, Simon T, Berthold F, Twist C, Schmidt ML, Castleberry RP, Matthay KK, Cohn SL, De Bernardi B (2005) The role of age in neuroblastoma risk stratification: the German, Italian, and children's oncology group perspectives. Cancer Lett 228:257–266

Manohar CF, Salwen HR, Brodeur GM, Cohn SL (1995) Co-amplification and concomitant high levels of expression of a DEAD box gene with MYCN in human neuroblastoma. Genes Chromosomes Cancer 14:196–203

Raggi CC, Bagnoni ML, Tonini GP, Maggi M, Vona G, Pinzani P, Mazzocco K, De Bernardi B, Pazzagli M, Orlando C (1999) Real-time quantitative PCR for the measurement of MYCN amplification in human neuroblastoma with the Taq-Man detection system. Clin Chem 45:1918–1924

Sano H, Bonadio J, Gerbing RB, London WB, Matthay KK, Lukens JN, Shimada H (2006) International neuroblastoma pathology classification adds independent prognostic information beyond the prognostic contribution of age. Eur J Cancer 42:1113–1119

Schmid SR, Linder P (1992) D-E-A-D protein family of putative RNA helicases. Mol Microbiol 6:283–291

Schmidt ML, Lal A, Seeger RC, Maris JM, Shimada H, O'Leary M, Gerbing RB, Matthay KK (2005) Favorable prognosis for patients 12 to 18 months of age with stage 4 nonamplified MYCN neuroblastoma: a Children's Cancer Group Study. J Clin Oncol 23:6474–6480

Scott D, Elsden J, Pearson A, Lunec J (2003a) Genes co-amplified with MYCN in neuroblastoma: silent passengers or co-determinants of phenotype? Cancer Lett 197:81–86

Scott DK, Board JR, Lu X, Pearson AD, Kenyon RM, Lunec J (2003b) The neuroblastoma amplified gene, NAG: genomic structure and characterisation of the 7.3 kb transcript predominantly expressed in neuroblastoma. Gene 307:1–11

Seeger RC, Brodeur GM, Sather H, Dalton A, Siegel SE, Wong KY, Hammond D (1985) Association of multiple copies of the N-myc oncogene with rapid progression of neuroblastomas. N Engl J Med 313:1111–1116

Shimada H, Umehara S, Monobe Y, Hachitanda Y, Nakagawa A, Goto S, Gerbing RB, Stram DO, Lukens JN, Matthay KK (2001) International neuroblastoma pathology classification for prognostic evaluation of patients with peripheral neuroblastic tumors: a report from the Children's Cancer Group. Cancer 92:2451–2461

Squire JA, Thorner PS, Weitzman S, Maggi JD, Dirks P, Doyle J, Hale M, Godbout R (1995) Co-amplification of MYCN and a DEAD box gene (DDX1) in primary neuroblastoma. Oncogene 10:1417–1422

Tajiri T, Tanaka S, Shono K, Kinoshita Y, Fujii Y, Suita S, Ihara K, Hara T (2001) Quick quantitative analysis of gene dosages associated with prognosis in neuroblastoma. Cancer Lett 166:89–94

Tanaka S, Tajiri T, Noguchi S, Shono K, Ihara K, Hara T, Suita S (2004) Clinical significance of a highly sensitive analysis for gene dosage and the expression level of MYCN in neuroblastoma. J Pediatr Surg 39:63–68

Tanner NK, Linder P (2001) DExD/H box RNA helicases: from generic motors to specific dissociation functions. Mol Cell 8:251–262

Vandesompele J, Speleman F, Van Roy N, Laureys G, Brinkschmidt C, Christiansen H, Lampert F, Lastowska M, Bown N, Pearson A, Nicholson JC, Ross F, Combaret V, Delattre O, Feuerstein BG, Plantaz D (2001) Multicentre analysis of patterns of DNA gains and losses in 204 neuroblastoma tumors: How many genetic subgroups are there? Med Pediatr Oncol 36:5–10

Weber A, Imisch P, Bergmann E, Christiansen H (2004) Coamplification of DDX1 correlates with an improved survival probability in children with MYCN-amplified human neuroblastoma. J Clin Oncol 22: 2681–2690

Available online at www.sciencedirect.com
ScienceDirect
Cancer Letters 247 (2007) 253–258
CANCER Letters
www.elsevier.com/locate/canlet

Marked and independent prognostic significance of the CpG island methylator phenotype in neuroblastomas ☆

Masanobu Abe [a,b], Frank Westermann [c], Akira Nakagawara [d], Tsuyoshi Takato [b], Manfred Schwab [c], Toshikazu Ushijima [a,*]

[a] *Carcinogenesis Division, National Cancer Center Research Institute, University of Tokyo Graduate School of Medicine, 5-1-1 Tsukiji, Chuo-ku, Tokyo 104-0045, Japan*
[b] *Department of Oral and Maxillo Facial Surgery, University of Tokyo Graduate School of Medicine, Japan*
[c] *Division of Tumor Genetics, German Cancer Research Center, Heidelberg, Germany*
[d] *Biochemistry Division, Chiba Cancer Center Research Institute, Japan*

Received 28 April 2006; accepted 2 May 2006

Abstract

The CpG island methylator phenotype (CIMP) was closely associated with poor overall survival (OS) in Japanese neuroblastoma (NBL) cases in our previous study. Here, in German NBL cases, CIMP(+) cases ($n = 95$) showed markedly poorer OS (hazard ratio (HR) = 9.5; $P < 0.0001$) and disease-free survival (DFS) (HR = 5.4; $P < 0.0001$) than CIMP(−) cases ($n = 50$). All the 23 cases with N-*myc* amplification had CIMP. Among the remaining cases without N-*myc* amplification, CIMP(+) cases ($n = 27$) had a poorer OS (HR = 4.5; $P = 0.02$) and DFS (HR = 5.2; $P < 0.0001$) than CIMP(−) cases ($n = 95$). In multivariate analysis, CIMP and N-*myc* amplification had an influence on OS and DFS independent of age and disease stage. CIMP had a stronger influence on DFS than N-*myc* amplification while N-*myc* had a stronger influence on OS.

Keywords: Neuroblastoma; Methylation; CIMP; MS-RDA; N-*myc*

1. Introduction

Neuroblastoma (NBL) is one of the most common pediatric solid tumors, and is characterized by two extreme disease courses, spontaneous regression and life-threatening progression. To implement adequate and necessary therapeutics, NBL cases are stratified into low-, intermediate- and high-risk groups based upon clinical and genetic information, such as disease stage, age at diagnosis, Shimada histology, N-*myc* amplification status, DNA ploidy, and *TrkA* expression level [1–6]. Especially, N-*myc* amplification, present in approximately 20–30% of NBL cases, is a powerful molecular marker for the stratification [1–4]. Nevertheless, more precise risk estimation is necessary for cases currently stratified

☆ A Grant-in-Aid for the Third-term Cancer Control Strategy Program from the Ministry of Health, Labour and Welfare (MHLW); and the Special Coordination Funds for Promoting Science and Technology from the Ministry of Education, Culture, Sports, Science and Technology (MEXT), Japan.
* Corresponding author. Tel.: +81 3 3547 5240; fax: +81 3 5565 1753.
E-mail address: tushijim@ncc.go.jp (T. Ushijima).

0304-3835/$ - see front matter © 2006 Elsevier Ireland Ltd. All rights reserved.
doi:10.1016/j.canlet.2006.05.001

into the intermediate-risk group, and development of a novel prognostic marker is awaited [1,2].

Recently, using a genome-wide screening method for differences in DNA methylation, methylation-sensitive representational difference analysis [7–9], we found that multiple CGIs were methylated in NBL cases with poor prognosis [10]. By analysis of 140 Japanese NBL cases, methylation of the multiple CGIs was shown to be dependent upon each other, and conformed to the concept of the CGI methylator phenotype (CIMP), originally established in colorectal cancers [11]. Cases could be classified as either CIMP(+) or CIMP(−), and a very limited number of cases had an intermediate phenotype. CIMP(+) cases had a markedly poorer overall survival (OS) than CIMP(−) cases with a hazard ratio (HR) of 22.1 [95% confidence interval (95%CI) = 5.3–93.4; $P < 0.0001$]. Its influence was independent of *TrkA* expression status, DNA ploidy, and age at diagnosis. Notably, almost all cases with N-*myc* amplification exhibited CIMP (37 of 38 cases), and, even among the cases without N-*myc* amplification, CIMP(+) cases had a poorer OS than CIMP(−) cases (HR = 12.4; 95%CI = 2.6–58.9; $P = 0.002$). CIMP status was well associated with the methylation level of the *Protocadherin β* (*PCDHB*) gene family, followed by methylation levels of *hepatocyte growth factor-like protein* (*HLP*) gene and *Cytochrome p450 CYP26C1* (*CYP26C1*).

Considering that there could be potential ethnic differences and that genome-wide screenings tend to produce "too good" results [12], here we took advantage of archived materials of German NBL cases. If the strong influence of CIMP on OS is also observed in German cases, we can establish CIMP as a prognostic marker that can be universally used. Also, the German NBL cases have information on disease-free survival (DFS), which was not available for Japanese NBL cases, and the influence of CIMP on DFS can be clarified.

2. Materials and methods

2.1. Tissue samples

A total of 152 cases were collected between 1998 and 2004, and all patients were enrolled in the German NBL Trial. The mean age at initial diagnosis was 1082 days (range 0–9607 days). Thirty-seven, 29, 17, 51 and 17 cases belonged to stages 1, 2, 3, 4, and 4S (International Neuroblastoma Staging System), respectively, although information was not available for one case. The composition of the cohort in terms of stage, N-*myc* status and age at diagnosis was in agreement with the composition of an unselected cohort of 1741 patients diagnosed between 1990 and 2003 in Germany [13]. DNA was extracted by the standard phenol/chloroform procedure, and used for this study under approval of Institutional Review Boards.

2.2. Sodium bisulfite modification and quantitative methylation-specific PCR (MSP)

One microgram of DNA restricted with *Bam*HI underwent sodium bisulfite modification [14], and was suspended in 20 μl of TE buffer. For quantitative MSP, 1 μl of the solution was used for PCR using SYBR Green PCR Core Reagents (PE Biosystems) and an iCycler Thermal Cycler (Bio-Rad Laboratories). PCR was performed separately for methylated (M) DNA molecules and for unmethylated (U) DNA molecules with primers specific to each sequence, and the numbers of M and U molecules in a test sample were determined by comparing their amplification with those of standard samples containing 10–10^6 molecules. Primer sequences and standard DNA were previously described [10]. The "methylation level" was calculated as the fraction of M molecules in the total DNA molecules (# of M molecules + # of U molecules). All the molecular analyses were performed blind to clinical information, and methylation level for a case was obtained as an average of two independent measurements.

2.3. Statistical analysis

Reproducibility of methylation levels between two measurements was assessed using the Pearson correlation coefficient. Survival time was measured from the date of initial diagnosis to the date of death or last contact. Kaplan–Meier analysis and log-rank tests were performed to compare overall survival (OS) and disease-free survival (DFS) between groups. HRs were estimated by the Cox proportional hazards model. These statistical analyses were performed using SPSS, version 13.0 (SPSS Inc., Chicago, IL).

3. Results

3.1. Determination of CIMP statuses in German NBL cases

Methylation levels were measured in 152 German NBLs for three CGI (group)s – (i) the 17 *PCDHB* family genes, (ii) *HLP*, and (iii) *CYP26C1*. They were highly reproducible with a correlation coefficient $\geqslant 0.99$, and the average levels were used hereafter. The methylation level of the *PCDHB* gene family showed a clear bimodal distribution (Fig. 1A). To avoid artificial bias, CIMP statuses were diagnosed before having access to clinical information of the cases. First, since cut-off values between 40% and 60% gave high HRs in our previous

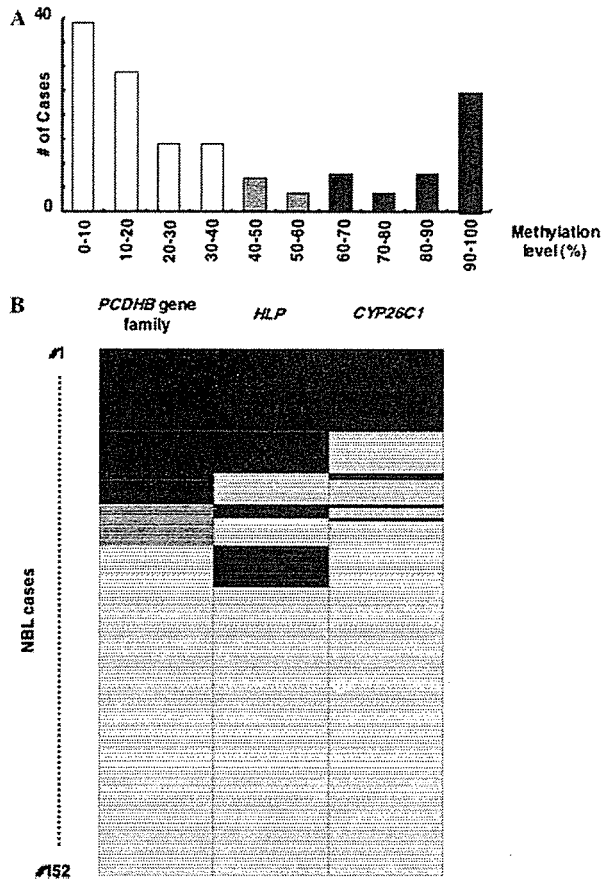

Fig. 1. Bimodal distribution of methylation levels of the *PCDHB* gene family, and diagnosis of CIMP status. (A) Histogram of number of cases according to *PCDHB* methylation levels. The methylation level of the *PCDHB* gene family was measured exactly as in our previous study [10], and its bimodal distribution in German NBLs was confirmed. (B) Methylation statuses of the three CGIs (groups) among the 152 NBLs. Cut-off values for the *PCDHB* gene family, *HLP* and *CYP26C1* were set based on the previous study, which were 40–60%, 10%, and 70%, respectively. Closed and open boxes show high and low methylation levels, and methylation levels of the *PCDHB* gene family between 40% and 60% are shown by grey boxes. Methylation levels of these three CGIs were closely associated with each other.

study [10], cases with methylation levels lower than 40% and higher than 60% were diagnosed as CIMP(−) ($n = 95$) and CIMP(+) ($n = 45$), respectively. Only 12 cases had methylation levels between 40% and 60%.

Then, for these 12 cases, methylation levels of *HLP* and *CYP26C1*, whose predictive powers followed that of the *PCDHB* gene family in our previous study [10], were taken into account. Five of the 12 cases had high levels of methylation of *HLP* and/or *CYP26C1*, and were considered to have CIMP, and seven other cases were left as unknown for CIMP status (Fig. 1B). Cut-off values for *HLP* and *CYP26C1* were set at the same levels as in our previous study, which were 10% and 70%, respectively. As a result, 50, 95, and 7 cases of the 152 cases were diagnosed as CIMP(+), CIMP(−), and unknown, respectively. Methylation statuses of the three CGI (groups) showed close correlation with methylation statuses of the other CGIs.

3.2. Univariate analysis with OS and DFS

In univariate analysis, the 50 CIMP(+) cases exhibited markedly and significantly poorer OS (HR = 9.5; 95%CI = 3.2–28.1; $P < 0.0001$) and DFS (HR = 5.4; 95%CI = 2.9–10.3; $P < 0.0001$) than the 95 CIMP(−) cases. Cases with N-*myc* amplification ($n = 23$) also exhibited markedly and significantly poorer OS (HR = 11.8; 95%CI = 4.9–28.7; $P < 0.0001$) and DFS (HR = 3.1; 95%CI = 1.6–6.0; $P = 0.0007$) than 122 cases without N-*myc* amplification. All of the 23 German cases with N-*myc* amplification had CIMP, as observed in a Japanese population.

Therefore, the German NBL cases were classified into three groups: (a) CIMP(−) cases ($n = 95$), all of which were without N-*myc* amplification, (b) CIMP(+) cases without N-*myc* amplification ($n = 27$), and (c) CIMP(+) cases with N-*myc* amplification ($n = 23$). As for OS (Fig. 2A), the three groups exhibited a step-wise increase of risk, showing the influence of N-*myc* amplification in addition to CIMP. Among the cases without N-*myc* amplification (groups (a) and (b)), CIMP had a significant influence on OS (HR = 4.5; 95%CI = 1.3–16.1; $P = 0.02$). As for DFS (Fig. 2B), CIMP had a significant influence (HR = 5.2; 95%CI = 2.6–10.6; $P < 0.0001$) by comparison of groups (a) and (b). However, additional influence by N-*myc* amplification was unclear by comparison of groups (b) and (c). These suggested that N-*myc* amplification had a strong influence on OS while CIMP had a strong influence on DFS.

3.3. Multivariate analysis

Since CIMP and N-*myc* amplification were dependent upon each other, multivariate analysis was first performed using age at diagnosis, disease stage, and either CIMP or N-*myc* amplification (Table 1A and B). It was confirmed that either CIMP or N-*myc* amplification had a significant influence on OS and DFS independent of age at diagnosis and disease stage.

Then, multivariate analysis was performed using age at diagnosis, disease stage, and both CIMP and N-*myc* amplification to compare the influences of them (Table 1C). As for OS, N-*myc* amplification retained its power while CIMP lost its power. In contrast, as for DFS, CIMP retained its power while N-*myc* amplification lost its power. This result was in accordance with the finding that CIMP had a strong influence on DFS while N-*myc* amplification had a strong influence on OS.

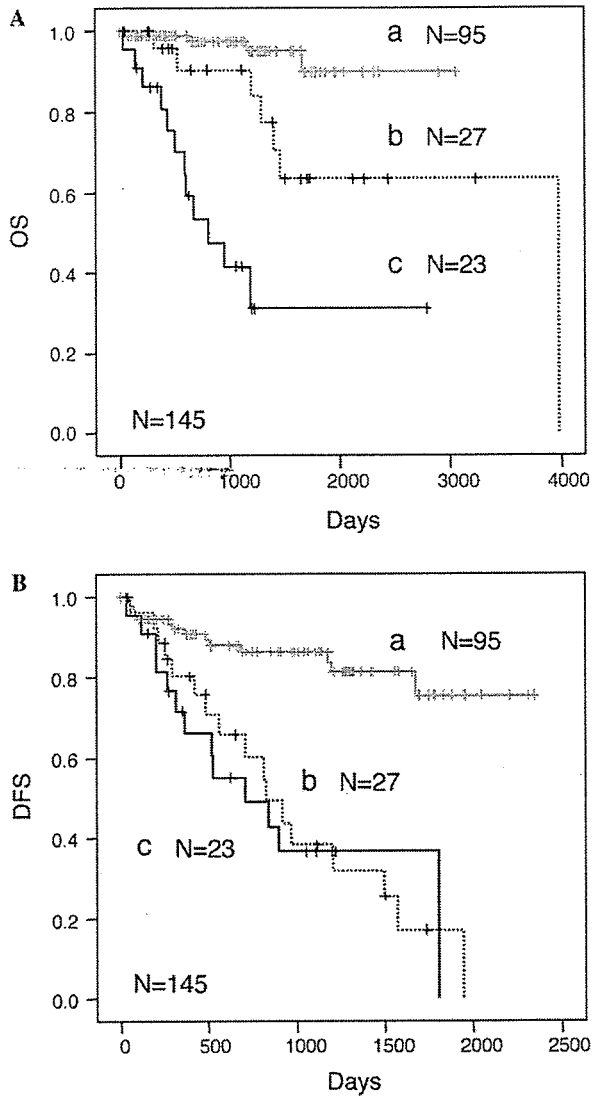

Fig. 2. Kaplan–Meier analysis of (a) CIMP(−) cases without N-*myc* amplification ($n = 95$), (b) CIMP(+) cases without N-*myc* amplification ($n = 27$), and (c) CIMP(+) cases with N-*myc* amplification ($n = 23$). (A) Kaplan–Meier analysis using OS. Using group (a) as a reference, group (b) had a HR of 4.5 (95%CI = 1.3–16.1; and $P = 0.02$), and group (c) had a HR of 21.7 (6.8–69.3; <0.0001). Using group (b) as a reference, group (c) had a HR of 4.8 (1.7–13.6; 0.003). (B) Kaplan–Meier analysis using DFS. Using group (a) as a reference, group (b) had a HR of 5.2 (2.6–10.6; <0.0001), and group (c) had a HR of 5.7 (2.6–12.2; <0.0001). There was no significant difference between groups (b) and (c) ($P = 0.82$).

4. Discussion

Methylation levels of the *PCDHB* gene family showed a bimodal distribution in German NBL cases, as in our initial analysis of Japanese NBL cases [10], and the presence of two groups of NBLs from the viewpoint of CIMP was confirmed. The CIMP statuses of individual German NBL cases were determined using criteria established in Japanese NBL cases to avoid falsely "too good" results, which tend to happen in genome-wide analyses [12]. Nevertheless, the strong influence of CIMP on OS in all the NBL cases (HR = 9.5) and also in those without N-*myc* amplification (HR = 4.5) was confirmed. After finishing all the analysis we searched for a *PCDHB* methylation level that would give the highest HR for the 152 German NBL cases, and it was 30% with a HR of 9.8 (95%CI = 2.9–33.0; $P < 0.0001$), followed by 40% with a HR of 9.4 (95%CI = 3.2–27.6; $P < 0.0001$). Based on the precise reproduction of the initial findings in Japanese NBL cases in German NBL cases, CIMP is highly likely to be a novel prognostic marker that can be universally used in cases without N-*myc* amplification. A prospective study is warranted.

A strong influence of CIMP on DFS was revealed for the first time in this study because data on DFS were available only for German NBL cases. In univariate analysis, CIMP had a strong influence on DFS in all the NBL cases (HR = 5.4) and in the cases without N-*myc* amplification (HR = 5.2) (groups (a) and (b) in Fig. 2B). In multivariate analysis involving age at diagnosis, disease stage, and both N-*myc* amplification and CIMP, CIMP retained its power on DFS while N-*myc* amplification retained its power on OS. This suggested that the recurrence of NBL cases was strongly associated with CIMP, but that NBL cases without N-*myc* amplification had higher chances to be induced into the second remission.

The almost complete inclusion of cases with N-*myc* amplification within the CIMP(+) cases in our two independent studies indicates that these two abnormalities are very closely associated with each other. If we assume a single abnormality that underlies a poor prognosis of NBL cases, it is likely that CIMP is caused by it, and some of CIMP(+) NBLs develop N-*myc* amplification. If we assume multiple abnormalities, it is likely that CIMP is consistently associated with the devastating status of NBLs, which can be induced by N-*myc* amplification and other causes. Clarification of what molecular abnormality causes CIMP and how CIMP and N-*myc* amplification are related is important.

The presence of CIMP was considered to lead to a poor prognosis by induction of methylation of promoter CGIs of various tumor-related genes. We

Table 1
Multivariate analysis of prognostic factors for overall and disease-free survival

Variable	OS			DFS		
	HR	95% CI for HR	*P*	HR	95% CI for HR	*P*
(A)						
Age at diagnosis	6.2	0.8–48.7	0.082	1.8	0.8–4.1	0.171
Disease stage	1.8	0.6–5.8	0.319	1.8	0.8–4.0	0.152
CIMP	4.9	1.5–15.8	0.008	3.3	1.5–7.0	0.002
(B)						
Age at diagnosis	13.6	1.8–104.3	0.012	2.5	1.1–5.6	0.025
Disease stage	1.5	0.5–5.0	0.501	2.6	1.2–5.4	0.013
N-*myc* amplification	11.5	3.9–33.8	<0.001	2.1	1.0–4.2	0.043
(C)						
Age at diagnosis	12.1	1.6–94.4	0.017	1.9	0.8–4.5	0.137
Disease stage	1.2	0.3–4.1	0.796	1.7	0.8–3.9	0.179
N-*myc* amplification	8.0	2.5–25.8	<0.001	1.3	0.6–2.7	0.563
CIMP	2.3	0.6–8.9	0.226	3.0	1.3–6.9	0.009

HR, hazard ratio; CI, confidence interval; OS, overall survival; DFS, disease-free survival.

previously observed association between CIMP and promoter methylation of tumor-suppressor *RASSF1A* and *BLU* genes [10]. It is reported that an anti-apoptotic gene, *TMS1*, a homeobox gene, *HOXA9*, a cell cycle gene, *CCND2*, and candidate tumor-suppressor genes, *EMP3* and *NR1I2*, are more frequently methylated in NBL cases with a poor prognosis [15–17]. However, the risk given by methylation of one of these individual genes is much smaller than that given by CIMP. This is in accordance with our hypothesis that CIMP leads to consistent methylation of marker CGIs, such as exonic CGIs of the *PCDHB* gene family, and occasional methylation of promoter CGIs of tumor-related genes. Silencing of an individual gene accounts for a poor prognosis of only a fraction of NBL cases with CIMP. It is known that exonic CGIs are more susceptible to methylation than promoter CGIs [9], and it is expected that they are more useful as a prognostic marker.

In summary, the faithful reproduction in German NBL cases of the highly significant findings obtained in Japanese cases demonstrated that CIMP is a strong and universal prognostic marker for NBL cases, especially for those without N-*myc* amplification. The close association between CIMP and DFS was revealed for the first time in this study.

Acknowledgments

The authors are grateful to Dr. S. Yamamoto for his advise on statistical analysis. The authors are especially grateful to the institutions that participated in the collection of clinical materials.

References

[1] M. Schwab, F. Westermann, B. Hero, F. Berthold, Neuroblastoma: biology and molecular and chromosomal pathology, Lancet Oncol. 4 (2003) 472–480.
[2] G.M. Brodeur, Neuroblastoma: biological insights into a clinical enigma, Nat. Rev. Cancer 3 (2003) 203–216.
[3] M. Schwab, K. Alitalo, K.H. Klempnauer, H.E. Varmus, J.M. Bishop, F. Gilbert, G. Brodeur, M. Goldstein, J. Trent, Amplified DNA with limited homology to *myc* cellular oncogene is shared by human neuroblastoma cell lines and a neuroblastoma tumour, Nature 305 (1983) 245–248.
[4] R.C. Seeger, G.M. Brodeur, H. Sather, A. Dalton, S.E. Siegel, K.Y. Wong, D. Hammond, Association of multiple copies of the *N-myc* oncogene with rapid progression of neuroblastomas, N. Engl. J. Med. 313 (1985) 1111–1116.
[5] Y. Kaneko, N. Kanda, N. Maseki, M. Sakurai, Y. Tsuchida, T. Takeda, I. Okabe, Different karyotypic patterns in early and advanced stage neuroblastomas, Cancer Res. 47 (1987) 311–318.
[6] A. Nakagawara, M. Arima-Nakagawara, N.J. Scavarda, C.G. Azar, A.B. Cantor, G.M. Brodeur, Association between high levels of expression of the *TRK* gene and favorable outcome in human neuroblastoma, N. Engl. J. Med. 328 (1993) 847–854.
[7] T. Ushijima, K. Morimura, Y. Hosoya, H. Okonogi, M. Tatematsu, T. Sugimura, M. Nagao, Establishment of methylation-sensitive-representational difference analysis and isolation of hypo- and hypermethylated genomic fragments in mouse liver tumors, Proc. Natl. Acad. Sci. USA 94 (1997) 2284–2289.
[8] A. Kaneda, D. Takai, M. Kaminishi, E. Okochi, T. Ushijima, Methylation-sensitive representational difference analysis and its application to cancer research, Ann. NY Acad. Sci. 983 (2003) 131–141.
[9] T. Ushijima, Detection and interpretation of altered methylation patterns in cancer cells, Nat. Rev. Cancer 5 (2005) 223–231.

[10] M. Abe, M. Ohira, A. Kaneda, Y. Yagi, S. Yamamoto, Y. Kitano, T. Takato, A. Nakagawara, T. Ushijima, CpG island methylator phenotype is a strong determinant of poor prognosis in neuroblastomas, Cancer Res. 65 (2005) 828–834.
[11] M. Toyota, N. Ahuja, M. Ohe-Toyota, J.G. Herman, S.B. Baylin, J.P. Issa, CpG island methylator phenotype in colorectal cancer, Proc. Natl. Acad. Sci. USA 96 (1999) 8681–8686.
[12] C. Tilstone, DNA microarrays: vital statistics, Nature 424 (2003) 610–612.
[13] W.B. London, L. Boni, T. Simon, F. Berthold, C. Twist, M.L. Schmidt, R.P. Castleberry, K.K. Matthay, S.L. Cohn, B. De Bernardi, The role of age in neuroblastoma risk stratification: the German, Italian, and children's oncology group perspectives, Cancer Lett. 228 (2005) 257–266.
[14] A. Kaneda, M. Kaminishi, T. Sugimura, T. Ushijima, Decreased expression of the seven ARP2/3 complex genes in human gastric cancers, Cancer Lett. 212 (2004) 203–210.
[15] M. Alaminos, V. Davalos, N.K. Cheung, W.L. Gerald, M. Esteller, Clustering of gene hypermethylation associated with clinical risk groups in neuroblastoma, J. Natl. Cancer Inst. 96 (2004) 1208–1219.
[16] M. Alaminos, V. Davalos, S. Ropero, F. Setien, M.F. Paz, M. Herranz, M.F. Fraga, J. Mora, N.K. Cheung, W.L. Gerald, M. Esteller, EMP3, a myelin-related gene located in the critical 19q13.3 region, is epigenetically silenced and exhibits features of a candidate tumor suppressor in glioma and neuroblastoma, Cancer Res. 65 (2005) 2565–2571.
[17] A. Misawa, J. Inoue, Y. Sugino, H. Hosoi, T. Sugimoto, F. Hosoda, M. Ohki, I. Imoto, J. Inazawa, Methylation-associated silencing of the nuclear receptor 1I2 gene in advanced-type neuroblastomas, identified by bacterial artificial chromosome array-based methylated CpG island amplification, Cancer Res. 65 (2005) 10233–10242.

RAPID COMMUNICATIONS IN MASS SPECTROMETRY
Rapid Commun. Mass Spectrom. 2007; **21**: 385–390
Published online in Wiley InterScience (www.interscience.wiley.com) DOI: 10.1002/rcm.2842

Resin-packed nanoelectrospray in combination with video and mass spectrometry for the direct and real-time molecular analysis of mast cells

Anusak Sirikatitham, Takahiro Yamamoto, Masakazu Shimizu, Tomomi Hasegawa, Naohiro Tsuyama and Tsutomu Masujima*

Analytical Molecular Medicine and Devices Laboratory, Graduate School of Biomedical Sciences, Hiroshima University, 1-2-3 Kasumi, Minami-ku, Hiroshima 734-8551, Japan

Received 16 May 2006; Revised 16 November 2006; Accepted 17 November 2006

A nano-electrospray ionization (nanoESI) emitter for analysis of a biological solution was developed by packing a nanoESI needle with two types of resins for desalting and preconcentration of target molecules. Determination of secreted histamine and serotonin molecules in cell culture buffers was demonstrated using 5-methyltryptamine as internal standard. The results showed good linearity of target signals in the concentration range from 0.25 to 50.0 ng/mL of histamine or serotonin. These molecules were monitored to be secreted by A23187 (calcium ionophore) stimulant in rat peritoneal mast cells. Using a combination of a video-microscope and a mass spectrometer, we could visualize exocytotic moments and analyze secreted molecules by mass spectrometry simultaneously. Time-dependent release of histamine and serotonin from activated mast cells showed that significant production of these molecules occurred and reached a maximal level at 15 min for serotonin and at 30 min for histamine, respectively. These results showed that this method allows the direct and timely analysis of secreted molecules in biological responses. Copyright © 2007 John Wiley & Sons, Ltd.

Video-image analysis[1,2] is the first step in the study of cell behavior; however, it does not provide any information about molecular contents and species in cells. Mass spectrometry (MS) has become a convenient tool for specifying compounds by their molecular weight, but it requires multiple purification steps of the analytes for precise analysis of cellular contents. Combination of a video-microscope and a mass spectrometer allows us to perform real-time analysis of cell behavior and analysis of molecular contents.[3] For that purpose, an appropriate pretreatment tool linked to an ionizing MS apparatus is required.

Rat peritoneal mast cells have been widely used as a model to study the release of allergic mediators. These cells have basic granules inside the cytoplasm which contain compounds such as histamine and serotonin. By adding stimulants, the granules in the cells are transported to the cell surface, and burst to release histamine and serotonin into the outside culture medium.[4–6] In order to measure these compounds using MS, it is essential to desalt and preconcentrate the target compounds on the microliter scale.

A number of sample-pretreatment techniques have been developed including liquid chromatography (LC),[7–10] capillary electrophoresis (CE),[11–13] capillary electrochromatography (CEC),[14–16] and microdialysis,[17] and they are usually used as an interface to introduce clean samples directly into the mass spectrometer. On the other hand, more efforts have been focused on the use of low flow rate approaches such as nano-electrospray ionization (nanoESI) techniques to reduce sample consumption and to yield smaller droplets for enhanced ionization efficiency.[18,19] There are several applications utilizing nanoESI needles for off-line and on-line experiments.[20–29] In both cases, biological samples must be pretreated before introduction into the mass spectrometer, such as desalting, deproteinization (if necessary) and preconcentration.

In the present study, we demonstrate the application of a resin-packed nanoESI needle interface that enables the coupling of a video-microscope with a mass spectrometer and can be applied successfully for the optimization of the low-level molecular contents analysis. Small, gold-coated nanoESI needles were integrally packed with two types of resin to provide preconcentration and desalting inside of the emitter itself and then these emitters readily give nanoESI of clean and concentrated samples for MS. Although resin-packed nanoESI emitters are commercially available (such as 'PicoFrit', New Objective Co.), in this case we targeted the preconcentration of amines which cannot be trapped by ODS resins. This emitter is well suited for generating a real-time interface for preconcentration and separation of amines and desalting and producing nanoESI.

*Correspondence to: T. Masujima, Analytical Molecular Medicine and Devices Laboratory, Graduate School of Biomedical Sciences, Hiroshima University, 1-2-3 Kasumi, Minami-ku, Hiroshima 734-8551, Japan.
E-mail: tsutomu@hiroshima-u.ac.jp
Contract/grant sponsor: Ministry of Education, Science, Sports and Culture of Japan.

RCM

EXPERIMENTAL

Materials

All chemicals used were purchased from several vendors: histamine dihydrochloride (Katayama Chemical, Osaka, Japan), 5-hydroxytryptamine hydrochloride, serotonin (Nacalai Tesque, Kyoto, Japan), and 5-methyltryptamine hydrochloride (Aldrich, St. Louis, IL, USA). Peritoneal mast cells were obtained from male mice, Sea:ddY model.

NanoESI needle fabrication

Borosilicate glass capillaries with 0.6 mm i.d. and 1.0 mm o.d. were used. They were pulled with a micropipette puller (model PB-7, Narishige, Tokyo, Japan) to make nanoESI needles with 2.2 μm diameter (RSD 8% (n = 5)) pore on its tapered end measured with an electron micrograph. A thin layer of gold was deposited on the circumference of the needles by ion sputtering (Fig. 1(a)).

Preparation of nanoESI emitter needles

The gold-coated nanoESI needles were cut to 25 mm length to fit microtubes, and filled with a few microliters of two types of resin. The resins were packed by putting the tapered edge of the needles at the bottom of the tubes using a low-speed centrifuge. First, a high-porosity reversed-phase resin (POROS R2, 20 μm diameter, Applied Biosystems, Foster City, CA, USA) was suspended in 75% MeOH (5 mg mL^{-1}) and 1.0 μL the of suspension was loaded into the needles using half-cut gel loading tips attached to micro-pipettes. The needles were settled into centrifuge adaptors which were placed into 1.5 mL microtubes, and centrifugation of the needles was performed at 2000 *g* for 3 min to pack the resin down to the tapered edge. The volume of the resin was estimated by measuring the length of the resin layer inside the needle using an optical microscope. Second, mixed-mode resin (cation-exchange and reversed-phase) (Oasis MCX, 30 μm diameter, Waters, Milford, MA, USA) was suspended in 75% MeOH (20 mg mL^{-1}), and 2.4 μL of slurry were then loaded into the needles followed by centrifugation resulting in the nanoESI emitter needles doubling as desalting and preconcentrating columns (Fig. 1(b)). The needles were only used once.

Mass spectrometer

All experiments were performed on an electrospray time-of-flight (TOF) mass spectrometer (Mariner, Applied Biosystems) with a custom mount that allows electrical contact to the gold-coated portion of the nanoESI needles. Neither nebulizer gas nor curtain gas was employed. Spray tip potential was 1000–1500 V and the nozzle potential was set at 100 V to obtain the best possible mass response. The nozzle temperature was 140°C. In the analysis of cell culture media, the positive ions ($[M+H]^+$) generated at *m/z* 112.2 and 177.1 (for histamine and serotonin, respectively) were detected and used for quantitative analysis.

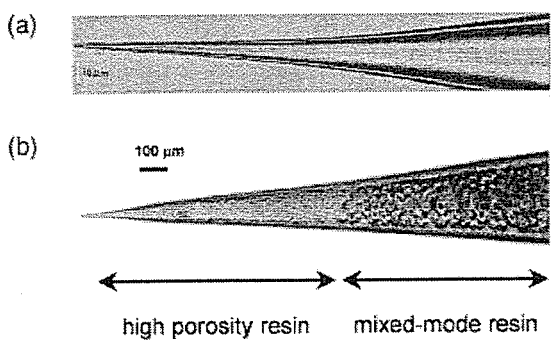

Figure 1. Glass needles for the nanoESI source: (a) nanoESI needle; 2 μm i.d. tip, made using the microcapillary puller and (b) gold-coated nanoESI needle packed with resins.

Recovery

The positively charged histamine and serotonin in acidified medium buffer loaded into resin-packed nanoESI needles were analyzed as described above, while they were also analyzed using unpacked needles for the control. The recovery from resin-packed nanoESI needles was calculated against the control. The recovery ratios were 88% and 93% for histamine and serotonin, respectively, at the concentration of 1.0 ng μL^{-1} (n = 3), as shown in Table 1. Thus this method demonstrated a satisfactory recovery for the real-time molecular contents analysis.

Mast cell analysis

Mast cells prepared from mouse peritoneum at a concentration of 10^4 cells/400 μL in modified Tylode-HEPES buffer (pH 7.4) according to a previous report[31] were stimulated with 5 mM calcium ionophore, A23187. The amounts of histamine and serotonin released from mast cells at various times after stimulation (0, 1, 5, 10, 15, 30 and 60 min) were measured as follows. An aliquot (40 μL) of the culture buffer was isolated, acidified with 2 μL of acetic acid, and then mixed with the internal standard, 5-methyltryptamine (final concentration: 1 ng/μL). It took around 2 min from isolating the culture buffer to adding the internal standard. Then 1.0 μL of acidified sample was loaded to the edge of the needles with the larger pore and then the needles were centrifuged which allows the samples to flow through the packed nanoESI needles to the tapered ends. The needles were then loaded with 3 μL of 1% acetic acid in 50% MeOH, and centrifuged briefly. These washing steps were repeated three times that allowed histamine and serotonin to be concentrated in the needles. Then, the needles were filled with a few milliliters of 2% ammonium hydroxide (NH_4OH) in 90% acetonitrile solution, and subsequently placed in the orifice of the TOF mass spectrometer. A potential of 1000–1500 V applied to the needles induced the spray of the samples which eluted the retained histamine and serotonin to give the TOF/MS for analysis. As the same amount of 5-methyltryptamine was added to all samples, the quantity of histamine and serotonin in each sample can be deduced using the calibration curves.

Table 1. Recovery of histamine and serotonin from packed nanoESI needles

Analyte	Concentration added (ng μL^{-1})	% Recovery	% RSD (n = 3)
Histamine	1.0	88	5
Serotonin	1.0	93	3

DOI: 10.1002/rcm

RESULTS AND DISCUSSION

Gold-coated nanoESI needles and their emitter performance

Gold-coated nanoESI needles were originally packed with high-porosity reversed-phase resin and mixed-mode (cation-exchange and reversed-phase) resin as shown in Fig. 1. These features are the essential parts of our nanoESI needle. Although the use of mixed-mode resin was the important part for purifying target compounds, its solitary use clogged the outlet of the needles because of the small pores in this resin; only 8 nm. Small pores in the resin disturbed the solvent flow at the very end of the tapered needles resulting in high back pressure at the end and lower stability of spray. To resolve this problem, high-porosity resin which yields smooth flow was initially packed to the very ends of the needles before packing with mixed-mode resin. Due to this combination of these two resins, back pressure inside the needles became minimal allowing continuous and copious spray during a set of analyses. In addition, application of mixed-mode resin for purification of basic compounds, histamine and serotonin, was effective as the recovery of these compounds was good. In addition, it was also important for desalting and concentrating the analytes to obtain clean samples for MS analysis.

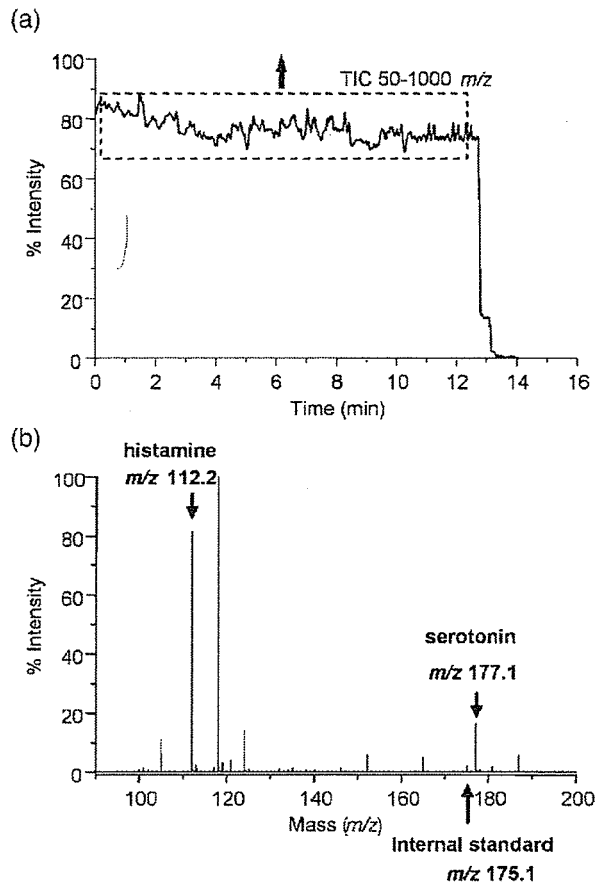

Figure 2. Total ion chromatogram (TIC, *m/z* 50–1000) of continuous nanoESI of histamine and serotonin eluted from a resin-packed nanoESI emitter with 2% NH_4OH in 90% acetonitrile. The enlarged average mass spectrum represents 10.0 ng of histamine and serotonin.

Gold is still the most commonly used conductive coating to provide voltage contact on nanoESI needles.[18,30] A potential of 1000–1500 V on the gold-coated and resin-packed nanoESI needles induces continuous spray at the flow rate of 70–80 nL min^{-1} using 1 μL of each sample. The total ion chromatograph (TIC, 50–1000 *m/z*, Fig. 2(a)) and the average mass spectrum (Fig. 2(b)) showed continuous nanoelectrospray of 10.0 ng histamine and serotonin in 1 μL of 2% NH_4OH in 90% acetonitrile as the eluting solvent. Thirteen minutes later, a drop in intensity was observed indicating that all the sample had been exhausted.

Clear mass signals of extracellular histamine (*m/z* 112.2) and serotonin (*m/z* 177.1) were obtained, and also other unknown signals from the buffer were detected (Fig. 2(b)). However, using buffer alone (negative control), the signals at *m/z* 112.2, 177.1 and 175.1 (internal standard) were not observed (data not shown).

Different concentrations of standard histamine and serotonin (0.25, 0.50, 1.0, 5.0, 10.0, 20.0 and 50.0 ng μL^{-1}) were prepared in modified Tyrode-HEPES buffer, treated according to the described procedure, and used to establish the calibration curves. The data were recalculated using an internal standard signal of 5-methyltryptamine (*m/z* 175.1) (1 ng μL^{-1}). In order to avoid matrix effects and to compensate for machine instability that affects ionization efficiency, all values were expressed as the ratio of mass response (counts) for histamine and serotonin to 5-methyltryptamine. The calibration curves were thus obtained, and they showed good linearity over the concentration range from 0.25–50.0 ng mL^{-1} (correlation coefficients, R^2, for histamine and serotonin were 0.995 and 0.993, respectively), as shown in Fig. 3. The signal is stable during the run (coefficient of variance (CV) 4 and 6% (n = 3) (within-run), and CV 6 and 7% (n = 3) (day to day) for histamine and serotonin, respectively) and the limits of detection for both histamine and serotonin were 0.01 ng/μL obtained with signal-to-noise (S/N) ratios of 3.5:1 and 4.7:1, respectively (data not shown).

These data suggested that the performance of the nanoESI needles was sufficient for our video and mass spectrometric analysis.

Video and mass spectrometric analysis

Using the combination of a video-microscope attached with a sampling device and a mass spectrometer, which we call combined video and mass spectrometry, we can inspect both cell dynamics and directly identify what types of compounds are produced and secreted by sampling intracellular or extracellular materials. Figure 4 illustrates schematically the operation of the system.

In the present technique, the extracellular material containing compounds released from the cells was taken. Culture buffer containing histamine and serotonin was acidified and introduced into the nanoESI needles. At low pH all basic compounds such as histamine, serotonin and 5-methyltryptamine were fully protonated and positively charged molecules were efficiently bound to the mixed-mode resin inside the needle. Then the needles were centrifuged to concentrate the samples and washed several times for desalting followed by elution of the trapped molecules.

DOI: 10.1002/rcm

RCM

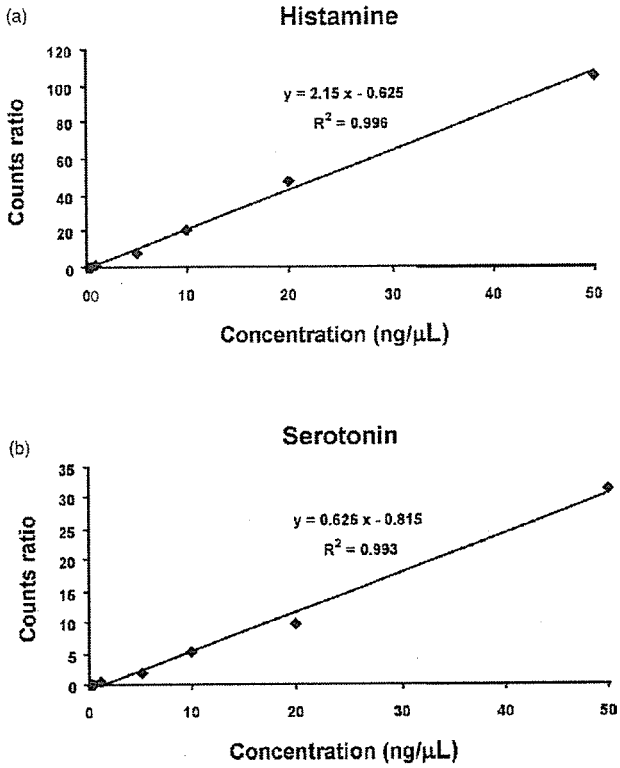

Figure 3. Calibration curves of histamine (a) and serotonin (b) in positive mode. The equations shown resulted from a linear regression fit to the ratio of the mass response (counts) of histamine and serotonin to 5-methyltryptamine (internal standard).

When the ESI voltage was applied to the needle, spray for mass spectral analysis resulted.

To assess the degree of mast cell activation following stimulation, histamine and serotonin release were evaluated. Figure 5(a) shows mast cells at the moment of secretion at various times after stimulation of A23187 (0, 1, 5, 10, 15, 30 and 60 min) using a video-microscope. Cell shape gradually became irregular compared to unstimulated cells, because a number of micro-granules were popped from mast cells. Subsequently, micro-granules were developed at the cell surface and the number of granules increased with time. However, the degree of excocytosis for each cell was not the same, because one cell in the middle exhibited fewer granules than the others. The representative mass spectra of the supernatant at various times are shown in Fig. 5(b). Histamine and serotonin peaks were clearly detected. The ratio of the mass response (counts) between the histamine and serotonin against 5-methyltryptamine (internal standard) was calculated and the concentrations of these compounds were calculated using the calibration curves.

The time-dependent release of histamine and serotonin by activated mouse peritoneal mast cells is shown in Fig. 6. Significant release of serotonin occurred at 15 min and histamine at 30 min after activation and reached a peak of approximately 128.6 ng/10^4 cells and 118.1 ng/10^4 cells, respectively, and gradually declined thereafter. It seems that this slow decline was due to the metabolism of histamine and serotonin, and that these compounds were taken back into cells. These data show that the time-course analysis of histamine and serotonin release from mast cells together with phenomenological observations are readily accomplished.

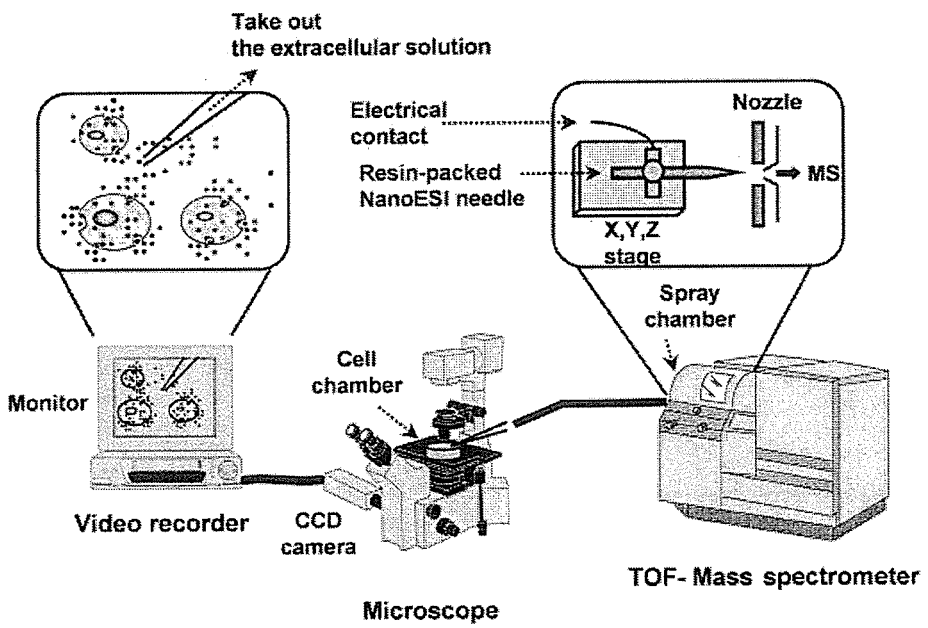

Figure 4. Schematic diagram of the 'Video and mass spectrometry' for real-time analysis of cell behavior. The culture buffer outside the mast cells under observation by the video-microscope was aspirated and acid-treated samples were introduced into the nanoESI interface of the TOF mass spectrometer.

DOI: 10.1002/rcm

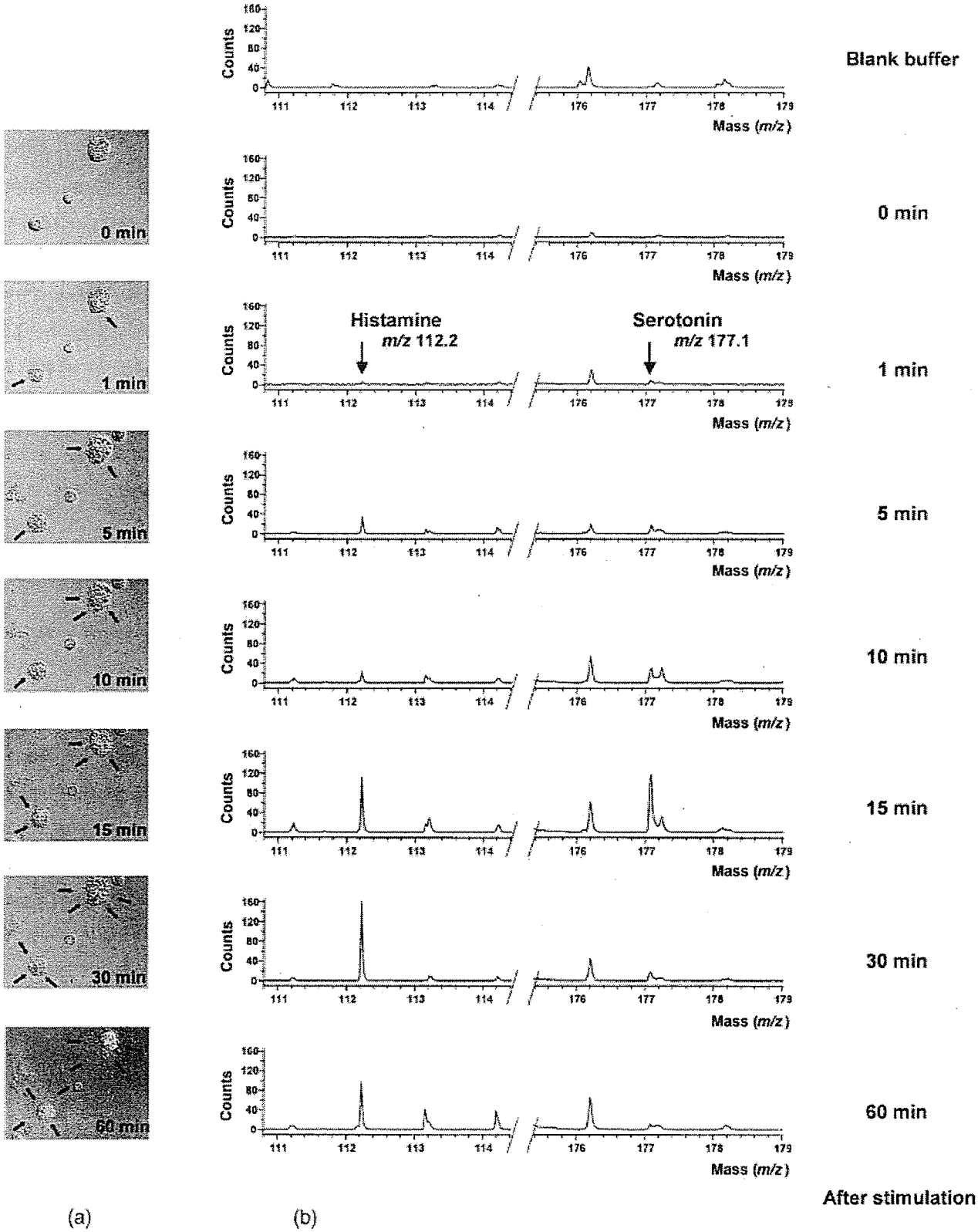

Figure 5. Time-course analysis of histamine and serotonin released from mast cells. (a) Sequential video images of peritoneal mast cells stimulated with A23187. Arrows indicate the points where the excretion of micro-granules from the cells occurred which include allergic mediators such as histamine and serotonin. (b) Representative nanoESI spectra of histamine (*m/z* 112.2) and serotonin (*m/z* 177.1) from cell culture. The arrows show the peaks of histamine and serotonin signals.

DOI: 10.1002/rcm

RCM

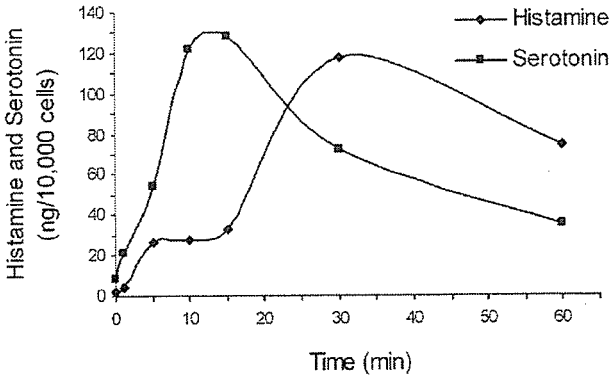

Figure 6. Time-dependent release of histamine and serotonin by activated mast cells. The amounts of histamine and serotonin were calculated using the calibration curves.

CONCLUSIONS

Nanoelectrospray ionization with our gold-coated and resin-packed nanoESI needles has become a unique bioanalytical strategy which enables the real-time analysis of histamine and serotonin in biological samples. The emitter needles can be packed with porous reversed-phase resin and mixed-mode chromatographic resin, thus facilitating preconcentration and desalting of amine-containing samples within the emitter itself prior to elution and MS analysis. Although the line is not connected to the sampling device of the microscope, the off-line disposable needles eliminate the need for a connecting system, and minimize the risk of contamination of the instrument. Advantages of these nanoESI needles include a low flow rate of 70–80 nL min^{-1} and small size of the spray emitter that reduce the required sample size and also promote the efficiency of ionization.

Thus, approaches using video and mass spectrometry will be more important for future analyses of time-dependent biological cell behavior and molecular content. Our nanoESI needles will be powerful tools for the analysis of biological samples using video and mass spectrometry.

Acknowledgements

This work was supported by Grants-in-Aid for Scientific Research from the Ministry of Education, Science, Sports and Culture of Japan.

REFERENCES

1. Chon JH, Vizena AD, Rock BM, Chaikof EL. *Anal. Biochem.* 1997; **252**: 246.
2. Bouchelouche PN. *Scand. J. Clin. Lab Invest. Suppl.* 1993; **214**: 27.
3. Masujima T. *Anal. Chim. Acta.* 1999; **400**: 33.
4. Bergendorff A. *Acta Physiol. Scand.* 1975; **95**: 133.
5. Siraganian RP, Kulczycki AJ, Mendoza G, Metzger H. *J. Immunol.* 1975; **115**: 1599.
6. Chasin M, Scott C, Shaw C, Persico F. *Int. Arch. Allergy Appl. Immunol.* 1979; **58**: 1.
7. Parker CE, Perkins JR, Tomer KB, Shida Y, O'Hara K. *J. Chromatogr.* 1993; **616**: 45.
8. Tomer KB, Moseley MA, Deterding LJ, Parker CE. *Mass Spectrom. Rev.* 1994; **13**: 431.
9. Davis MT, Stahl DC, Lee TD. *J. Am. Soc. Mass Spectrom.* 1995; **6**: 571.
10. Allen JR, Williams JD, Burinsky DJ, Cole SR. *J. Chromatogr. A* 2001; **913**: 209.
11. Nilsson S, Markides KE. *Rapid Commun. Mass Spectrom.* 2000; **14**: 6.
12. Chang YZ, Her GR. *Anal. Chem.* 2000; **72**: 626.
13. Li J, Tremblay TL, Wang C, Attiya S, Harrison DJ, Thibault P. *Proteomics* 2001; **1**: 975.
14. Choudhary G, Horvath C, Banks JF. *J. Chromatogr. A* 1998; **828**: 469.
15. Strickmann DB, Blaschke G. *J. Chromatogr. B Biomed. Sci. Appl.* 2000; **748**: 213.
16. Walhagen K, Gaspari M, Tjaden UR, Rozing GP, Greef J. *Rapid Commun. Mass Spectrom.* 2001; **15**: 878.
17. Liu C, Hofstadler SA, Bresson JA, Udseth HR, Tsukuda T, Smith RD, Synder AP. *Anal. Chem.* 1998; **70**: 1797.
18. Wilm M, Mann M. *Anal. Chem.* 1996; **68**: 1.
19. Thomas R. *Spectroscopy* 2001; **16**: 26.
20. Valaskovic GA, Kelleher NL, Little DP, Aaserud DJ, McLafferty FW. *Anal. Chem.* 1995; **67**: 3802.
21. Fligge TA, Bruns K, Przybylski M. *J. Chromatogr. B* 1998; **706**: 91.
22. Davis MT, Lee TD. *J. Am. Soc. Mass. Spectrom.* 1998; **9**: 194.
23. Maziarz EP 3rd, Lorenz SA, White TP, Wood TD. *J. Am. Soc. Mass Spectrom.* 2000; **11**: 659.
24. Pont F, Luciani B, Belmant C, Fournie JJ. *Anal. Chem.* 2001; **73**: 3562.
25. Wetterhall M, Nilsson S, Markides KE, Bergquist J. *Anal. Chem.* 2002; **74**: 239.
26. Shen Y, Zhao R, Berger SJ, Anderson GA, Rodriguez N, Smith RD. *Anal. Chem.* 2002; **74**: 4235.
27. Ishihama Y, Rappsilber J, Andersen JS, Mann M. *J. Chromatogr. A* 2002; **979**: 233.
28. Lee SS, Douma M, Koerner T, Oleschuk RD. *Rapid Commun. Mass Spectrom.* 2005; **19**: 2671.
29. Luo Q, Shen Y, Hixson KK, Zhao R, Yang F, Moore RJ, Mottaz HM, Smith RD. *Anal. Chem.* 2005; **77**: 5028.
30. Nilsson S, Svedberg TM, Pettersson J, Bjorefors TF, Markides K, Nyholm L. *Anal. Chem.* 2001; **73**: 4607.
31. Levi-Schaffer F, Austen KF, Caulfield JP, Hein A, Bloes WF, Stevens RL. *J. Immunol.* 1985; **135**: 3454.

DOI: 10.1002/rcm

Computer Simulations of a New Three Rods Ion Optic (TRIPOLE) with High Focusing and Mass Filtering Capabilities

Gary Abdiel Salazar and Tsutomu Masujima
Analytical Molecular Medicine and Devices Laboratory, Graduate School of Biomedical Sciences, Hiroshima University, Hiroshima, Japan

A novel three rod (tripole) ion optic to which three AC voltages with symmetrically delayed phase shifts were applied to each electrode. We studied its ion guiding, focusing, and mass filtering capabilities by SIMION ver. 7.0 computer simulations. An electric field mathematical model was developed to calculate the pseudopotential of the tripole radial AC force. The tripole showed stable ion guiding for wide ranges of AC amplitude; better collisional focusing than hexapole and octapole and similar focusing as quadrupole (rod pole). Also, the ion optic clearly showed interesting mass filtering potential when the phase shift was asymmetrically delayed. The symmetric shape of the pseudopotential field explained the tripole ion guiding and focusing capabilities. For mass filtering, the pseudopotential was asymmetric and its effect was balanced with DC voltage to separate the ions, depending in their masses. The resolution was much lower than quadrupole but useful when rough filtering was required. (J Am Soc Mass Spectrom 2007, 18, 413–421) © 2007 American Society for Mass Spectrometry

Ion guide and ion focusing devices are essential in mass spectrometry. For example, the beam must be focused into the small differential pumping apertures for high ion transmission. The resolution and transmission of a not-well-focused ion beam through a quadrupole decreases because many ions are randomly lost due to imperfect fields located near the electrodes [1]. Similar situation of focused beam affects the resolution of the orthogonal time-of-flight mass spectrometer [2]. Mass selection is the heart of mass spectrometry and the quadrupole has governed AC voltage mass filtering for a long time, but science should continue the search for new and less expensive filters.

We are introducing an ion optic with three AC poles, hereafter named as "tripole," with better collisional focusing capabilities than hexapole and octapole. Also, the tripole showed interesting mass filtering potential.

Ion Guiding and Collisional Focusing

In AC ion guides the ions can be confined in radial dimension due to the presence of inhomogeneous AC field [3]. Under certain conditions, ion motion in any inhomogeneous AC field can be described by the pseudo or effective potential theory [3–9]. If the ion loses kinetic energy due to inelastic collisions with neutral gas particles, it will move to areas of low pseudopotential located near the center [10]. The pseudopotential can be calculated and expressed as electric potential with the eq 1 (Dehmelt, H. G., equation) [11].

$$\psi = (e/4m\omega^2)E_0^2 \quad (1)$$

where m is the ion mass (kg), e is the ion charge (Coulombs), ω is the AC voltage frequency in rad/s, and E_0 is the amplitude of the AC electric field.

Collisional focusing in 2D guides has been useful since it was established [12], and its strength can be critical for capturing ions with high mass and high initial velocity distribution. For example, with a QqTOF instrument, high mass proteins have been well detected in intact form [13]. Also, MALDI time-of-flight signals for Alzheimer biomarkers have been improved [14]. Efficient ion guides with inert or reactive gas are necessary and useful in collision-induced dissociation (CID) and inductively coupled plasma (ICP) reaction cells [15, 16].

Experimental

Conventional and Novel AC Ion Optic

Looking for new ion optics with simple electrode arrangements and high collisional focusing, we are introducing a new AC-ion optic-like multipole that consists of three parallel cylindrical electrodes equally aligned in radial symmetry around the central z-axis, defining an inscribed space with radius (r_0). Three AC voltages, symmetrically delayed to phase shifts of 0, 120, and 240 degrees are applied to each electrode with the aim of creating a rotational electric field, see Figure 1. For understanding and predicting the tripole guiding, focusing, and filtering capabilities; we studied the ion

Published online December 4, 2006
Address reprint requests to Dr. T. Masujima, Humanix, Hiroshima University, 1-2-3 Kasumi, Minami-ku, Hiroshima City, Hiroshima 734-8551, Japan.E-mail: tsutomu@hiroshima-u.ac.jp

1044-0305/07/$32.00
doi:10.1016/j.jasms.2006.10.007

Received May 2, 2006
Revised October 11, 2006
Accepted October 16, 2006

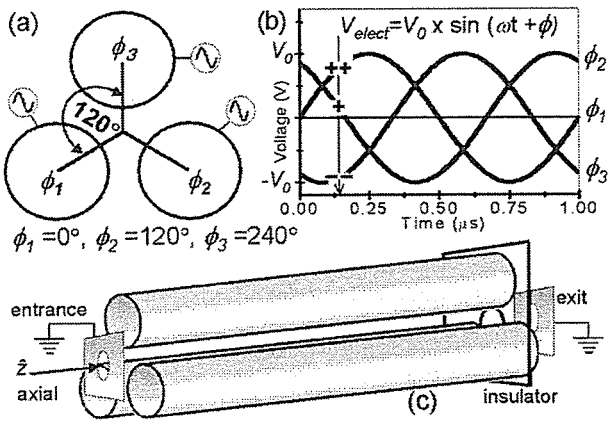

Figure 1. Tripole scheme. (a) Tripole cross-section with symmetric rod positioning; (b) three AC voltages with phase shift applied to each rod; (c) 3D view with entrance and exit metal apertures, and insulator plate. The insulator is used only when using the tripole as mass filter.

movement inside this novel arrangement by computer simulations and by calculating its pseudopotential field.

The electric potential (V) in polar coordinates can be easily calculated for multipoles:

$$V(r,\ \theta,\ t) = V_0(r/r_0)^N\cos(N\theta)\cos(\omega t) \text{ and}$$
$$|E_0| = NV_0/r_0(r/r_0)^{N-1} \quad (2)$$

where V_0 is the zero to peak AC voltage amplitude, r_0 is the field radius, and N is the number of pairs of parallel rods [17]. A mathematical model for the tripole radial electric potential and pseudopotential was developed because calculating the pseudopotential from SIMION data is an impractical and very time-consuming method that only SIMION users can reproduce. Tripole potential will be a complicated mixture of many other multipoles, each with similar amplitude.

Also, calculations of collisions with background gas were added to the simulations, to study collisional focusing and compare with conventional guides. Because the stability diagram is the essence of mass filtering, we would like to find the tripole DC-AC ion stability ranges to find a mass filtering behavior.

Computational Methods

Tripole Pseudopotential Mathematical Model

For the tripole, an electric field mathematical model was developed by fitting the electric field calculated with SIMION ver. 7.0 3D. SIMION SL TOOLS software was used to convert the SIMION data (binary format) in numerical format for the tripole 2-D array "main body," explained in "Ion Movement Simulations."

Ion Guiding

The AC voltages and ion-gas collisions were controlled by SIMION user-programming. For computer memory saving, the tripole was segmented in three "array instances" (entrance, main body, and exit). The segments were proportionally scaled by changing the software array density (*mm/gu*), where *mm* is millimeter and *gu* is the software arbitrary distance unit [18]. We chose the instances array density thinking in a balance between computational time and simulation accuracy. The entrance instance was a 3D electric potential array with density of 0.04167 times r_0 (0.04167x r_0) *mm/gu*; rods length 108 *gu*, the ratio of the electrodes (r_e) with r_0 was r_e/r_0 = 2.2; and an entrance plate with dimensions (212 × 212 × 6) *gu*, separated 10 *gu* from the rods. Groups of 25 ions, radially positioned around the central axis, were flown individually from inside of a through-hole (radius r_0) in the entrance plate. The main body instance was a 2D array with density of 0.00833 *mm/gu* times r_0, centered on the central axis. The 2D main body was projected in the z-axis as 3D planar symmetry by controlling the "nz" parameter, until obtaining the tripole total length (150 mm). The exit instance of the tripole was exactly equal to the entrance instance, including an exit plate.

The conventional multipoles (quadrupole, hexapole, and octapole) simulation parameters were similar to the tripole but they were divided only in two array instances, entrance and main body. The multipoles entrance and main body array density were equal as for tripole but the proportion of the electrode radius with the inscribed space radius (r_e/r_0) for hexapole was 0.5375, for octapole 0.355, and for quadrupole 1.130 [19, 20].

Mass Filtering

The SIMION simulation was similar as in the section "ion guiding" because the tripole mass filter scheme was almost equal to the tripole ion guide. The differences were: DC voltage was applied to electrode "1" and the AC voltage phase shift of electrode "1" and "2" were studied, searching for mass filtering behavior. An insulator plate (2 mm thick) with a through-hole of radius (r_0) centered on the longitudinal axis was placed at the edge of the tripole end, just before the exit plate. The beam initial conditions were: groups of 25 ions were flown together with kinetic energy 10 ± 10% eV, elevation angle el = ±5°, azimuthal angle az = ±90°, initial position y = ±0.05 mm, x = ±0.05 mm from the center, and the initial time-of-birth delay was 0 < TOB < 0.9 μs. Trying to simulate real ion beams, the initial conditions were randomized using the algorithm included in SIMION package demonstrations.

Theory and Calculation

Collisional Focusing Model

We chose the ion/neutral hard sphere collision model developed by Dahl, D. [21]. In our work, the gas particle speed was fixed at the root mean square of the Maxwell-Boltzmann distribution (V_{rms}) instead of ran-

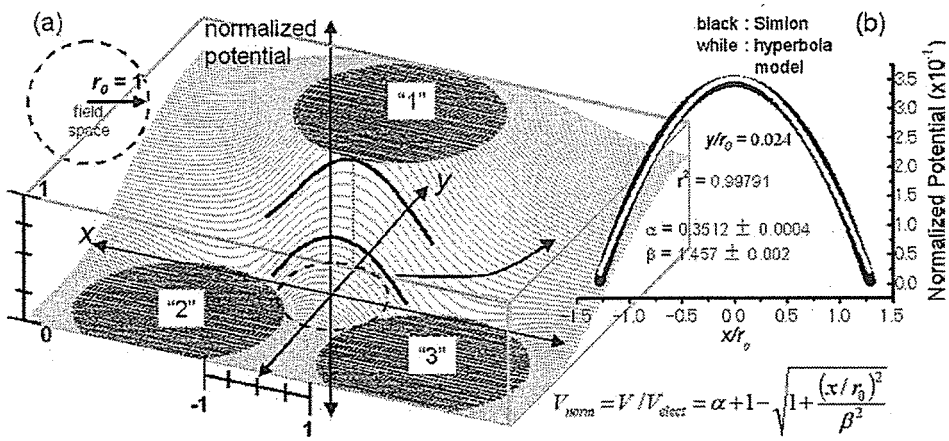

Figure 2. Tripole electric potential surface in cartesian coordinates calculated by SIMION. (a) The potential has been normalized to the potential of the electrode "1" and the cartesian coordinates has been normalized to the field radius (r_0); (b) hyperbolic shape of the normalized potential at a fixed y/r_0 position, highly fitted with the proposed mathematical model.

domly distributing it. This model includes approaches that simulate real systems such as thermal broadening, scattering angle, "rear-end," and "head-on" elastic collisions. The ion-gas collision cross-sections were approximated by $\sigma = K \times m^b$ [22]. The constants K and b, 2.41Å^2 and 0.664, respectively, were obtained by fitting the cross section values from the mass dependent database of Valentine et al. [23], and ion mass "m" is in Daltons.

Tripole Normalized Electric Potential Curve and Electric Field

By numerical analysis of the electric potential, calculated by SIMION, we developed and fitted a mathematical model. Figure 2 represents the electric potential surface of tripole cross-section with electrode field radius ratio (r_e/r_0) of 2.2, with positive voltage applied to the electrode "1," and the others are grounded. The x-y Cartesian coordinates were normalized over r_0 (x/r_0, y/r_0) and the electric potential values were normalized over the voltage of electrode "1" ($V1/V1_{elect}$).

Numerical Analysis of the Normalized Potential Curve

Let us approach the curve of normalized electric potential versus x/r_0 position, at any determined y/r_0 position inside the field space (see Figure 2), with a modified hyperbola equation written as eq 3. The hyperbola canonical equation was modified by fixing the root to negative and by adding the factor (α + 1). These modifications fix the vertex in the V-y plane and its direction will depend on the electrode voltage polarity, α will be equal to the normalized potential at the vertex, and β will be proportional to the hyperbola width.

$$V_\eta = V/V_{elect} = \alpha + 1 - \sqrt{1 + \frac{(x/r_0)^2}{\beta^2}} \quad (3)$$

Eq 3 was applied to 25 hyperbolas, located at different y/r_0 positions from −1 to 1, for the tripole electric field (r_0 = 3 *mm*, $V1_{elect}$ = 100 V). One typical example of the eq 3 fitting is shown in Figure 2b and the average

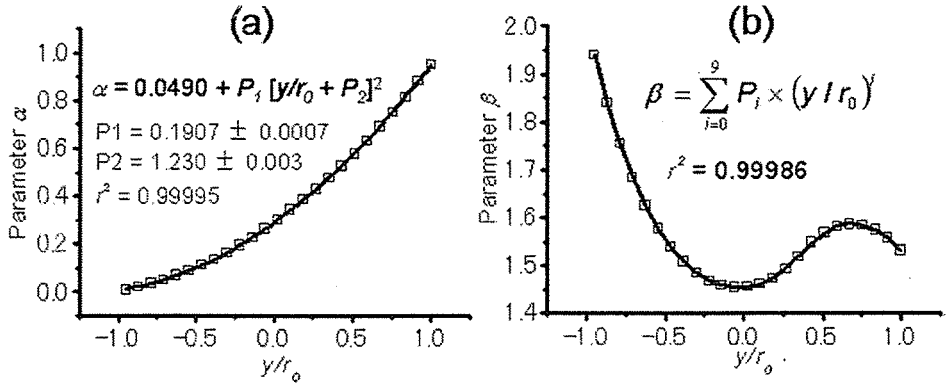

Figure 3. Hyperbola model parameters for tripole electric field, n = 25. (a) α Parameter with quadratic behavior; (b) β parameters with polynomial behavior.